

LEO-PNT With Starlink: Development of a Burst Detection Algorithm Based on Signal Measurements

Winfried Stock, Christian A. Hofmann, and Andreas Knopp

Institute of Information Technology, University of the Bundeswehr Munich, Neubiberg, Germany
papers.sp@unibw.de

Abstract—Due to the strong dependency of our societies on Global Navigation Satellite Systems and their vulnerability to outages, there is an urgent need for additional navigation systems. A possible approach for such an additional system uses the communication signals of the emerging LEO satellite mega-constellations as signals of opportunity. The Doppler shift of those signals is leveraged to calculate positioning, navigation and timing information. Therefore the signals have to be detected and the frequency has to be estimated. In this paper, we present the results of Starlink signal measurements. The results are used to develop a novel correlation-based detection algorithm for Starlink burst signals. The carrier frequency of the detected bursts is measured and the attainable positioning accuracy is estimated. It is shown, that the presented algorithms are applicable for a navigation solution in an operationally relevant setup using an omnidirectional antenna.

Index Terms—LEO, Starlink, navigation, signals of opportunity

I. INTRODUCTION

At least since the widespread use of smartphones, Positioning, Navigation and Timing (PNT) functionalities have become a matter of course in the everyday lives of very many citizens. Additionally, in the context of Industry 4.0 the importance of PNT has been increasing drastically for industry, agriculture, etc. in the last few years. Most devices that offer PNT functionality rely on Global Navigation Satellite Systems (GNSS). Due to some deficiencies of GNSS, e.g., when used in cities or forests and in jamming scenarios, there is an urgent need for additional systems. Plans for including PNT functionalities in the future 6G standard for cellular networks underline this need.

A promising approach for an additional navigation system uses Signals of Opportunity (SoO). Such systems use signals that are not designed or transmitted for the purpose of navigation but make secondary use of already available signals. The advantage of an SoO approach is that no dedicated transmitters have to be operated. On the downside, the structure of the utilized signals is not optimized for PNT and is often unknown.

In the previous decades, especially terrestrial signal sources, such as cellular basestations, were considered as SoO. With the New Space movement and the exponentially growing number

The authors are with the SpaceCom Labs of the Space Systems Research Center, Bundeswehr University Munich, 85579 Neubiberg, Germany (e-mail: papers.sp@unibw.de). This research is partly funded by dtec.bw – Digitalization and Technology Research Center of the Bundeswehr. dtec.bw is funded by the European Union - NextGenerationEU.

of LEO satellites in operation, the signals of LEO satellites have become more and more interesting as a source for an SoO navigation approach (LEO-PNT). Several characteristics of LEO satellites make them a promising source: There are LEO satellite signals available all the time on the whole globe, and the orbits of the satellites are known through the TLE files published by the North American Aerospace Defense Command (NORAD). Additionally, LEO satellites move with high velocity (relative to, e.g., a terrestrial receiver), which (over time) causes a fast changing geometry. Furthermore, a considerable Doppler shift is caused, which can be leveraged for PNT. In such an approach, PNT information is derived from frequency measurements of the received signal (similar to the measurement of the time of arrival of GNSS signals and the calculation of PNT information by triangulation).

This paper focuses on using Starlink signals as SoO for a LEO-PNT system. Since 2018, the Starlink system has been continuously growing and is now the constellation with the largest number of operational satellites in the LEO [2]. Hence, Starlink is a suitable candidate to provide SoO for LEO-PNT.

However, until recently, very little was known about the structure of Starlink signals. For this reason, so far, the published opportunistic LEO-PNT implementations have leveraged rather superficial signal properties, like the bandwidth, peaks in the frequency domain, and an assumed periodicity of the signal [3]–[6]. Due to the recent publication of an in-depth analysis of the Starlink user downlink signal in [7], dedicated Starlink signal detection and frequency estimation algorithms can be developed that utilize the exact signal structure and might offer a significantly higher estimation accuracy.

In this work, the basic working principles of Doppler shift based LEO-PNT are described. The Starlink user uplink signal is measured and analyzed. To the knowledge of the authors, this work is the first one doing so. Similarities between the uplink and downlink signal structures are identified. Algorithms for burst detection and frequency estimation that utilize the Starlink synchronization sequence are proposed and analyzed. Finally, the impact of the frequency estimation errors of those algorithms on the positioning accuracy of Doppler shift based LEO-PNT is investigated by calculating its lower bound.

II. OPPORTUNISTIC LEO-PNT

The basic working principle of an opportunistic LEO-PNT receiver leveraging the Doppler shift of LEO communication signals is depicted in figure 1. After an initial filtering and

arXiv:2304.09535v1 [eess.SP] 19 Apr 2023

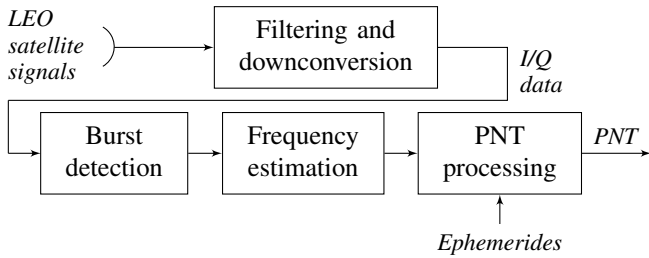


Fig. 1: Generic receiver architecture for Doppler shift based LEO-PNT

downconversion, the LEO burst signal is detected, and a carrier frequency estimation is conducted. Subsequently, PNT information is calculated from the received carrier frequency f_r and the location and velocity of the satellite. This calculation is possible because the high relative velocity between the transmitting satellite and the receiver causes a significant Doppler shift f_D , which depends on the relative position between the satellite and receiver. The velocity and location of the satellite are usually obtained from the ephemerides made public by NORAD in TLE files [8]. Strategies to identify the individual satellite (to match the transmitting satellite and the TLE file) have to be applied. As the signal properties of individual satellites are usually not known publicly, those strategies are, for example, based on preknowledge of the approximate receiver position. In the following, this section provides a better understanding of PNT calculation from frequency measurements.

During the overflight of a satellite, the changing relative velocity between transmitter and receiver causes a characteristic evolution of the Doppler shift over time. The precise shape of this Doppler shift curve depends on the receiver position relative to the satellite trajectory. Figure 2 shows some examples for different locations in cross-track direction \vec{x}_c of a static receiver on the earth surface. Different locations in along-track direction \vec{x}_a produce the same Doppler shift curves, but time-shifted. (\vec{x}_a refers to the direction parallel to the ground track of the satellite; \vec{x}_c is perpendicular to \vec{x}_a and parallel to the earth surface.) Mathematical models to calculate the Doppler shift can be found, e.g., in [10].

When the signal of a single satellite is tracked over the timespan t_a , commonly, an opportunistic LEO-PNT receiver estimates (at least some of) the following parameters: the receiver's 3D-position, the receiver's 3D-velocity, the receiver time, and the transmitted carrier frequency. The last parameter can also include the (possibly time-varying) clock drifts of the satellite and the receiver. The number of conducted frequency measurements N must at least match the number of parameters that are estimated by the receiver. However, the higher the number of measurements, the more accurate the PNT estimation is. The same is true for t_a . A longer tracking duration t_a entails measurements with a greater variety of geometry between satellite and receiver, which improves accuracy. For the same reason, the PNT estimation accuracy can be significantly

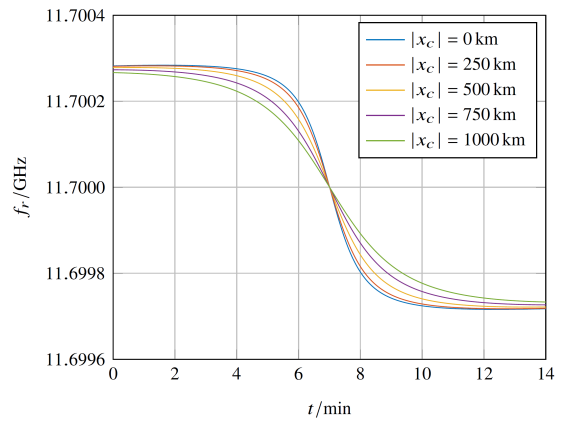


Fig. 2: Received center frequency f_r for different receiver positions in cross-track direction during a satellite overflight

improved by conducting measurements from several satellites with different orbits.

Several sources introduce errors to Doppler shift based PNT estimation. Among the most significant sources are the following three. First, the orbit of the satellite is not known exactly. The TLE files published by NORAD entail satellite position errors of up to a few kilometers [11]. Second, errors are introduced by the clocks of the receiver and of the satellite. The latter cannot be assumed to have an accuracy comparable to those of GNSS. (This, e.g., results in time varying carrier frequency offsets or sampling frequency offsets.) Last, the frequency estimation introduces errors. While the first-mentioned sources are not in the scope of this work, Section V will focus on the impact of the last-mentioned error source on the positioning accuracy.

III. STARLINK SIGNAL MEASUREMENTS

This section provides an overview of the Starlink signals. At first, a signal model is presented that fits the user uplink as well as the user downlink signal. After that, the uplink signal is described based on signal measurements and analysis conducted in the course of this work. Finally, the downlink signal is described shortly based on the in-depth analysis provided very recently by [7].

A. Signal model

Due to similarities in their structure, the same signal model can be applied for Starlink uplink and downlink signals:

$$s_i[n] = \alpha(c_i[n] + d_i[n - L_c])e^{j2\pi(f_{c_i} + f_{D_i})T_s n} + w[n] \quad (1)$$

where $s_i[n]$ is the i -th received signal burst at the n -th time instant. The data signal in baseband is denoted by $d_i[n]$, the noise term by $w[n]$, and $T_s = \frac{1}{f_s}$ denotes the sampling period. The carrier frequency f_{c_i} depends on the used subchannel and, therefore, can vary from burst to burst. The received signal bursts are shifted in frequency by f_{D_i} , which includes the Doppler shift as well as (at least for uplink signals) the Doppler shift pre-compensation applied by the transmitter. Within each

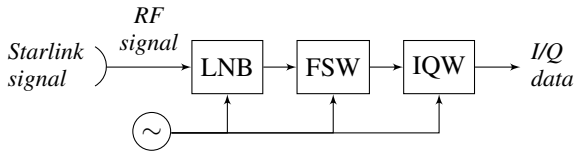


Fig. 3: Signal measurement setup

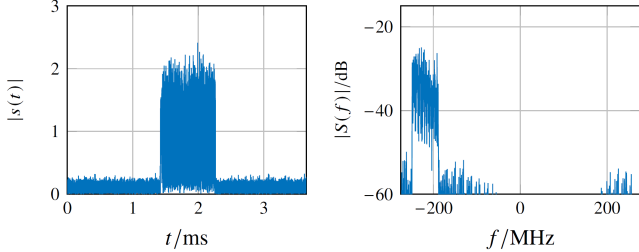


Fig. 4: Exemplary Starlink uplink burst in time and frequency domain in baseband

burst, f_{D_i} is assumed to be constant. The complex channel gain α describes all channel effects except the Doppler shift. The baseband synchronization sequence $c_i[n]$ with length L_c and $n \in \{0, \dots, L_c - 1\}$ can be described by

$$c_i[n] = \dot{c}^p + \sum_{k=0}^7 \dot{c}_i^k [n - (k + \gamma)\dot{L}_c] \quad (2)$$

where \dot{c}_i^k denotes the k -th subsequence with $k \in \{0, 1, \dots, 7\}$. Each subsequence has a length of \dot{L}_c samples. The relationship between those elements can be described with $-\dot{c}_i^0 = \dot{c}_i^1 = \dot{c}_i^2 = \dots = \dot{c}_i^7$. The prefix \dot{c}_i^p is a cyclic prefix of \dot{c}_i^0 and consists of $\gamma\dot{L}_c$ samples. As c_i is assumed to be the same for each burst, the index i can be omitted.

B. Uplink signal properties

Conducted measurements: In the course of this work, Starlink user uplink signal measurements were conducted with the setup depicted in figure 3. A horn antenna was placed next to an active Starlink user terminal. The received signal was amplified and downconverted in a low noise block downconverter (LNB). A R&S®FSW spectrum analyzer and R&S®IQW wideband I/Q data recorder were used to downconvert the signal to (quasi) baseband and store it. The equipment was synchronized by a 10 MHz rubidium oscillator. The stored signal was analyzed in MATLAB®. The investigated signal has a duration of 80 s and a sampling rate of $f_s = 562.500.000 \text{ s}^{-1}$.

The signal analysis shows, that the vast majority of the bursts (8519 of 8776 revealed bursts) have a bandwidth of around $B_{us} = 62.5 \text{ MHz}$, which corresponds to one of eight subchannels within the uplink bandwidth B_u . It is noticeable that large blocks of consecutive bursts use the same subchannel. The rare but regular changes in the used subchannel could be explained by a handover between different satellites that use different subchannels.

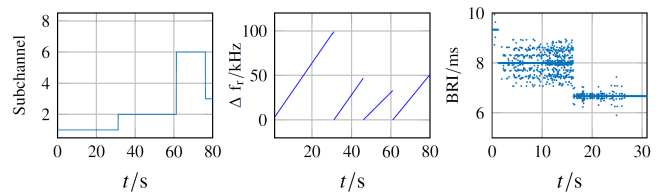


Fig. 5: Subchannel, relative carrier frequency, and BRI over the time of detection of each burst

For the Burst Repetition Time (BRI), defined as the time between the beginning of consecutive bursts, of a large majority of the bursts, it seems to apply $\text{BRI} \in \{6.67 \text{ ms}, 8.00 \text{ ms}, 9.33 \text{ ms}, 10.67 \text{ ms}, 16.00 \text{ ms}, 18.67 \text{ ms}\}$. The subchannels of the bursts with bandwidth B_{us} are shown in figure 5, as well as the BRI of those bursts in subchannel 1 (14.0 GHz – 14.0625 GHz). (Very few bursts with higher BRIs are not shown.) The burst duration seems to be highly variable. While some durations, like, e.g., 0.84 ms, are frequently used, the duration seems to be adaptable in timesteps of 17.87 μs . The rough estimation of the received carrier frequency Δf_r (relative to the frequency of the first burst in the same subchannel) shows that the user terminal applies Doppler shift pre-compensation to the uplink signal.

Correlation based analysis: To further investigate the signal, the following correlation algorithm is established: for two complex signals $y_1[n]$ with $n \in \{0, \dots, L_{y_1}\}$ and $y_2[n]$ with $n \in \{0, \dots, L_{y_2}\}$ and $L_{y_1} > L_{y_2}$ the correlation r_{y_1, y_2} can be calculated with

$$r_{y_1, y_2}[l] = \frac{1}{A} r'_{y_1, y_2}[l] = \frac{1}{A} \sum_{n=0}^{L_{y_1}} y_1[n] y_2^*[n - l] \quad (3)$$

where $(\cdot)^*$ represents the complex conjugate of a complex value. The normalization factor A is given by

$$A = \sqrt{r'_{\hat{y}_1, \hat{y}_1}[0] r'_{y_2, y_2}[0]} \quad (4)$$

where \hat{y}_1 is the part of y_1 with length L_{y_2} that starts with index $\hat{l} = \max\{r'_{y_1, y_2}\}$.

The structure of the uplink signal was determined by explorational calculations of (3) with different parts of s_i .

With the given sampling rate f_s , the parameters of the structure can be specified as $\dot{L}_c = 1200$ and $\gamma\dot{L}_c = 220$. The correlations in figure 6 between a burst signal s_i and the first element of the synchronisation sequence of the same burst c_i^1 were calculated with those values and validate the findings.

Further analysis shows that a small number of different correlation sequences c seem to be used in the uplink. Which specific sequence is used appears to be mainly connected to the burst's BRI and the subchannel and therefore presumably the satellite. However, more than 70% of the bursts in subchannel 1 seem to use one of three different correlation sequences. Additionally, the maximum correlation coefficients between different bursts do not significantly exceed 0.8 in most cases. This indicates that even for what above is considered to be

the same correlation sequence c indeed is not exactly the same sequence. Furthermore, in some bursts, the relationship between the phase of the transmitted elements c^k is not as described in the section above and seems unpredictable.

C. Downlink signal properties

This section sums up the analysis from [7] as far as they are relevant for this work. For Starlink user downlink signals, 2 GHz of bandwidth are allocated. Each Starlink beam uses one of 8 subchannels with bandwidth $B_d = 240$ MHz. In time domain, the downlink signal is composed of consecutive bursts s_i , which are thus called frames, with length $T_f = 1.3\bar{3}$ ms. Every frame starts with a synchronisation sequence c , which has the exact structure described in the signal model above. Each of the eight subsequences c^k are identical for every burst and satellite, except that the first subsequence and the cyclic prefix are inverse. The subsequences are $T_{c^k} = 4.27$ μ s in length, use the entire bandwidth of a subchannel B_d , and are made up of 127 (known) DPSK-modulated symbols. The relative length of the prefix c^p is $\gamma = 1/32$. The data signal d_i includes 302 OFDM-like symbols. Aside from the synchronisation sequence c , the first, last, and (in parts) the second to last of the 302 OFDM-like symbols are constant and appear to be used for synchronisation as well.

IV. BURST DETECTION AND FREQUENCY ESTIMATION

In this section, an algorithm for Starlink burst detection and a two-step algorithm for frequency estimation are presented. Those algorithms are correlation-based and utilize the synchronization sequence c . The properties of the presented algorithms are discussed using the Starlink uplink signal.

A. Burst detection algorithm

The presented burst detection algorithm adds up the magnitude of eight partial correlations between the received signal s and a representative ϵ . The latter is a measured or reproduced copy of c_i , consisting of subsequences ϵ^k and a prefix ϵ^p .

$$d_{s,\epsilon}[l] = \frac{1}{D} \sum_{k=0}^7 |d_{s,\epsilon}^k[l]| \quad (5)$$

$$d_{s,\epsilon}^k[l] = \sum_{n=0}^{L_s} s[n] \epsilon^k[n - (\gamma + k)\hat{L}_c - l]^* \quad (6)$$

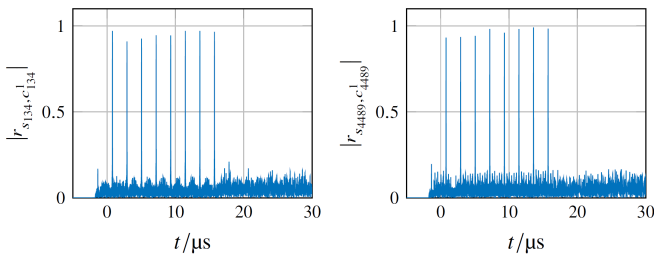


Fig. 6: Correlation r_{s_i, c_i^1} for two exemplary bursts

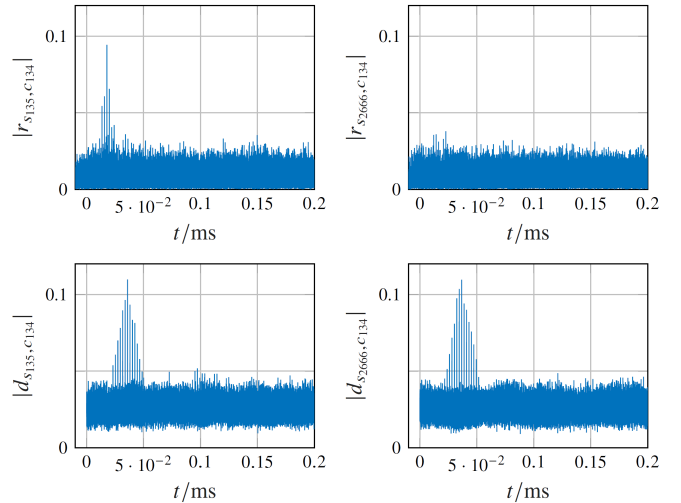


Fig. 7: Correlation results $r_{s,\epsilon}$ and $d_{s,\epsilon}$ for consecutive and non-consecutive bursts for SNR = -20 dB

The normalization factor D is defined analogous to A in (4). A burst is detected at sample l_j , if $d_{s,\epsilon}[l_j]$ exceeds a certain threshold and is the maximum value within a certain signal duration $T > L_c T_s$.

B. Frequency estimation algorithm

The carrier frequency estimation of a burst detected at sample l_j is conducted with a two-step algorithm. In a first step, a raw frequency estimation is calculated by determining the maximum value of $r_{s,\epsilon}[l_j]$ when different frequency shifts Δf are applied to ϵ [13].

$$\tilde{f}_j = \max_{\Delta f} \{r_{s,\epsilon}[l_j]\} \quad (7)$$

$$\epsilon_{\Delta f}[n] = \epsilon e^{j2\pi\Delta f T_s n} \quad (8)$$

In a second step, a fine carrier frequency estimation is performed using results from (6).

$$\hat{f}_j = \frac{1}{2\pi\hat{L}_c T_s} \arg \left\{ \sum_{k=1}^7 \left(d_{s,\epsilon}^{k-1}[l_j] \cdot d_{s,\epsilon}^k[l_j]^* \right) \right\} + \frac{g_j}{\hat{L}_c T_s} \quad (9)$$

The correction factor $g_j \in \mathbb{Z}$ accounts for the $\frac{1}{L T_s}$ ambiguity of this algorithm. Results from (7) can be used to calculate g_j . The estimator (9) is based on an estimator from [13], which meets the Cramér-Rao bound (CRB).

C. Algorithm analysis with Starlink uplink signals

The presented algorithms are applied to the measured Starlink uplink signal, which contains different synchronization sequences. Therefore, the calculations are conducted with three different representatives ϵ_1 , ϵ_2 , and ϵ_3 .

When comparing the presented detection algorithm to a simple correlation-based approach, some properties are noticeable. First, the results $d_{s,\epsilon}$ are significantly less susceptible to an unknown carrier frequency offset or Doppler shift in

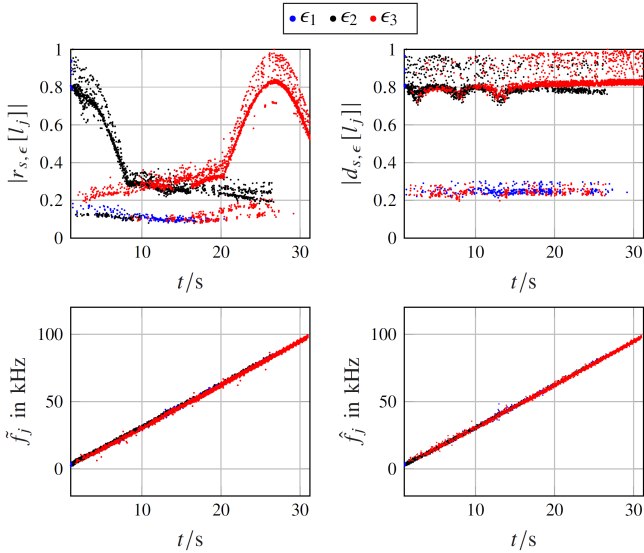


Fig. 8: Detections with $r_{s,\epsilon}$ and $d_{s,\epsilon}$ and frequency estimations with \tilde{f}_j and \hat{f}_j for all bursts in subchannel 1

the received signal than the results of a simple correlation $r_{s,\epsilon}$. This is observed from figure 7, where the algorithms are calculated for consecutive and non-consecutive bursts. When the burst used as a representative and the burst under investigation are transmitted within a short time period, (nearly) the same Doppler shift pre-compensation is applied to both. Otherwise, significantly different pre-compensations are applied, resulting in a significant decrease in the magnitude of $r_{s,\epsilon}$. The same conclusion can also be derived from figure 8, which shows $r_{s,\epsilon}$ and $d_{s,\epsilon}$ at the samples l_j , where bursts are detected. For improved clarity, only the results with the best fitting representative for each burst are presented. Furthermore, the results in figure 7 show that $r_{s,\epsilon}$ suppresses the (added Gaussian-distributed) noise better due to a higher correlation gain. However, $r_{s,\epsilon}$ is significantly more computationally expensive than $d_{s,\epsilon}$.

Frequency estimation results are presented in figure 8, as well. Again, only the frequency estimations with the representative with the best detection properties ($d_{s,\epsilon}[l_j]$) are considered there. Also, as the representatives are not in baseband, the results contain a frequency offset.

V. POSITIONING ACCURACY ESTIMATION

In the following section, the achievable positioning accuracy is calculated. As a first step, the available SNR at the receiver antenna output is estimated. Thereafter, a lower bound of the frequency estimation error is presented. Consequently, the resulting error for Doppler shift based positioning is derived. It is important to mention that additional error sources like, e.g., the ephemeris errors are not considered here.

Assumptions about the SNR: With simple transformations of equations from [14] the SNR_r at the receiver antenna output

can be calculated with

$$\text{SNR}_r = \frac{\Phi_t \lambda_c^2 G_r}{4\pi k_B T_N} \quad (10)$$

where Φ_t is the spectral flux density of the transmitted signal, describing the power per surface area and per wavelength, λ_c is the carrier wavelength of the downlink signal, and G_r is the receiver antenna gain. The Boltzmann constant is denoted by k_B , the noise temperature by T_N .

Carrier frequency offset estimation: When estimating the carrier frequency offset ν of the received signal, the estimation accuracy is lower bounded by the modified Cramér-Rao bound (MCRB) from [13]

$$\text{MCRB}(\nu) = \frac{3}{T_b^2 2\pi L_0^3} \frac{1}{\text{SNR}_r} \quad (11)$$

with the symbol duration T_b , and observation duration $L_0 T_s$.

Positioning estimation: As a last step, PNT information is calculated from the conducted frequency measurements. Therefore, N measurements with zero-mean, independent, Gaussian distributed measurement errors with variance σ^2 are assumed. Additionally, a static receiver with known altitude x_h , and unknown longitude x_l and latitude x_b (in geodetic coordinates) is assumed. In accordance with [15], for this scenario the CRB can be specified as

$$\text{CRB}_{x_l, x_b} = \sigma^2 \text{tr}((H^T H)^{-1}) \quad (12)$$

where $\text{tr}(\cdot)$ represents the trace of a matrix. The matrix H is defined as

$$H = \begin{bmatrix} \frac{\partial f_1(x_l, x_b)}{\partial x_l} & \dots & \frac{\partial f_N(x_l, x_b)}{\partial x_l} \\ \frac{\partial f_1(x_l, x_b)}{\partial x_b} & \dots & \frac{\partial f_N(x_l, x_b)}{\partial x_b} \end{bmatrix}^T \quad (13)$$

with $f_1(x_l, x_b), \dots, f_N(x_l, x_b)$ being the received carrier frequencies (including Doppler shift) at the N time instances the measurements were conducted.

Results for tracking a single Starlink satellite: Equations (10-13) are now used to calculate the lower bound of the positioning error. The MCRB(ν) from (11) is used as variance σ^2 in (12). The received frequencies $f_1(x_l, x_b), \dots, f_N(x_l, x_b)$ are calculated using the spherical-earth model from [16], omitting the earth rotation.

The following scenario is assumed: a receiver tracks a single Starlink satellite for the timespan t_a and estimates the frequencies $f_n \in \{f_1, \dots, f_N\}$ of the synchronization sequences c at time instances $t_n = qT_f$ with $q \in \{-\frac{N-1}{2}, \dots, \frac{N}{2}\}$. $T_f = \frac{1}{750}$ s is the repetition time at which Starlink transmits the synchronization sequence. Assuming that the full synchronization sequence of the Starlink user downlink signal is used, the symbol duration is $T_b = 4.17 \times 10^{-9}$ s and the number of observed symbols is $L_0 = 8 \cdot 127$ [7]. The satellite passes the zenith at $t = 0$ s at an orbit with height $x_{h,s} = 550$ km. The transmitted carrier frequency is $f_c = 11.7$ GHz, the spectral flux density is assumed to be $\phi_t = -122$ dB/m²/MHz. This is the maximum value at the ground according to Starlink's FCC filing [17].

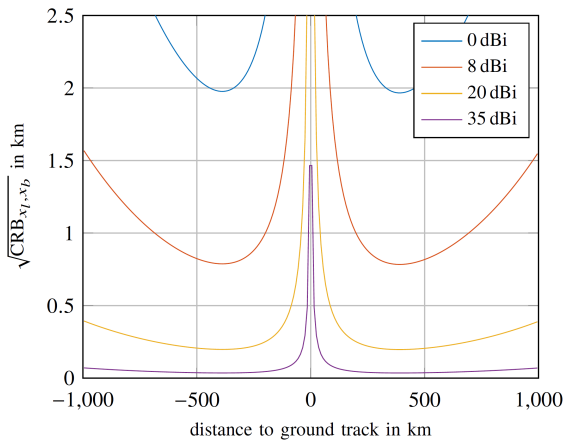


Fig. 9: Lower bound for the standard deviation of the positioning error for different values of G_r when $t_a = 4$ min

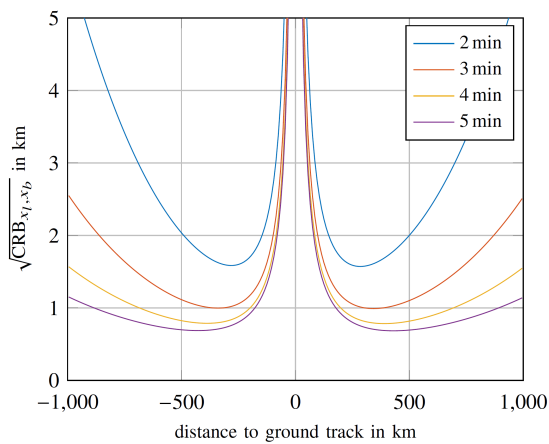


Fig. 10: Lower bound for the standard deviation of the positioning error for different values of t_a when $G_r = 8$ dB

Figure 9 shows the lower bound of the positioning accuracy for the tracking timespan $t_a = 4$ min for different receiver antenna gains. For a simple patch antenna with, e.g., $G_r = 8$ dB, the results show a positioning error of less than 1 km for a distance of 200 - 700 km between the receiver and the ground track of the satellite. For smaller distances the accuracy deteriorates rapidly due to inaccuracies in cross-track direction. For larger distances, the estimation in along-track direction is the dominant error source. Figure 10 shows the impact of the tracking timespan t_a on the positioning accuracy. Depending on Starlink's beamsteering protocol the maximum timespan to receive and track the main lobe signal of a satellite might be limited.

VI. CONCLUSION

In this work, measurement results of the Starlink user uplink signal are analyzed. Each burst's synchronization sequence is found to consist of 8 repetitions of the same subsequence. Thereby, the identified uplink structure showed significant similarities to the Starlink user downlink signal. Algorithms

that utilize the Starlink synchronization sequence for burst detection and frequency estimation are proposed and analyzed by applying them to the Starlink uplink signal. It is shown that the presented detection algorithm is very robust against an unknown carrier frequency offset or Doppler shift in the received signal. The presented frequency estimation is computationally efficient and promises an estimation variance near the lower bound. Finally, the impact of frequency estimation errors on the positioning accuracy of Doppler shift based LEO-PNT is investigated by calculating its lower bound. When the Starlink synchronization sequence is used for frequency estimation of a single satellite overflight, the induced positioning errors for most measurement scenarios are in the order of kilometers. Strategies to improve the accuracy include conducting measurements from different satellites with different orbits, using highly directional antennas, and utilizing more parts of the Starlink burst for frequency estimation.

REFERENCES

- [1] Z. M. Kassas, J. Khalife, A. Abdallah, and C. Lee, "I am not afraid of the jammer: Navigating with signals of opportunity in gps-denied environments," *Proceedings of the 33rd International Technical Meeting of the Satellite Division of The Institute of Navigation (ION GNSS+ 2020)*, pp. 1566–1585, 10 2020.
- [2] M. Wall, "Watch spacex launch 51 starlink internet satellites on jan. 15 after delays." [Online]. Available: <https://www.space.com/spacex-launch-starlink-group-2-4>
- [3] M. Neinavaie, J. Khalife, and Z. M. Kassas, "Exploiting starlink signals for navigation: First results," in *Proceedings of the 34th International Technical Meeting of the Satellite Division of The Institute of Navigation (ION GNSS+ 2021)*, 10 2021, pp. 2766–2773.
- [4] —, "Acquisition, doppler tracking, and positioning with starlink leo satellites: First results," *IEEE Transactions on Aerospace and Electronic Systems*, vol. 58, pp. 2606–2610, 6 2022.
- [5] M. Neinavaie, Z. Shadram, S. Kozhaya, and Z. M. Kassas, "First results of differential doppler positioning with unknown starlink satellite signals," in *2022 IEEE Aerospace Conference (AERO)*. IEEE, 3 2022, pp. 1–14.
- [6] J. Khalife, M. Neinavaie, and Z. Z. Kassas, "The first carrier phase tracking and positioning results with starlink leo satellite signals," *IEEE Transactions on Aerospace and Electronic Systems*, vol. 58, pp. 1487–1491, 4 2022.
- [7] T. E. Humphreys, P. A. Iannucci, Z. Komodromos, and A. M. Graff, "Signal structure of the starlink ku-band downlink," *arXiv*, 10 2022.
- [8] North American Aerospace Defense Command (NORAD), "Two-line element sets." [Online]. Available: <http://celestrak.org/NORAD/elements/>
- [9] R. W. Middlestead, *Digital Communications with Emphasis on Data Modems*. Hoboken, NJ, USA: John Wiley & Sons, Inc., 3 2017.
- [10] M. L. Psiaki, "Navigation using carrier doppler shift from a leo constellation: Transit on steroids," *NAVIGATION*, vol. 68, pp. 621–641, 9 2021.
- [11] Z. Kassas, M. Neinavaie, and J. Khalife, "Enter leo on the gnss stage: Navigation with starlink satellites," *Inside GNSS*, pp. 42–51, 11 2021.
- [12] C. A. Hofmann and A. Knopp, "Ultrabroadband waveform for iot direct random multiple access to geo satellites," *IEEE Internet of Things Journal*, vol. 6, no. 6, pp. 10 134–10 149, 2019.
- [13] U. Mengali and A. N. D'Andrea, *Synchronization Techniques for Digital Receivers*. Boston, MA: Springer US, 1997.
- [14] A. F. Molisch, *Wireless Communications*, 2nd ed. Wiley Publishing, 2011.
- [15] F. Guo, Y. Fan, Y. Zhou, C. Xhou, and Q. Li, *Space Electronic Reconnaissance: Localization Theories and Methods*. Wiley, 6 2014.
- [16] X. Chen, M. Wang, and L. Zhang, "Analysis on the performance bound of doppler positioning using one leo satellite," *2016 IEEE 83rd Vehicular Technology Conference (VTC Spring)*, pp. 1–5, 5 2016.
- [17] FCC filing, "Spacex non-geostationary satellite system, attachment a, technical information to supplement schedule s," 2018.